

# Fluid-acoustic interactions in self-sustained oscillations in turbulent cavity flows. I. Fluid-dynamic oscillations

Hiroshi Yokoyama<sup>1,a)</sup> and Chisachi Kato<sup>2</sup>

<sup>1</sup>Graduate School of Engineering, The University of Tokyo, 7-3-1 Hongo, Bunkyo-ku, Tokyo 113-8656, Japan

<sup>2</sup>Institute of Industrial Science, The University of Tokyo, 4-6-1 Komaba, Meguro-ku, Tokyo 153-8505, Japan

(Received 25 March 2009; accepted 18 September 2009; published online 23 October 2009)

The fluid-acoustic interactions in a flow over a two-dimensional rectangular cavity are investigated by directly solving the compressible Navier–Stokes equations. The upstream boundary layer is turbulent. The depth-to-length ratio of the cavity is 0.5. Phase-averaged flow fields reveal the mechanism for the acoustic radiation. Large-scale vortices form in the shear layer that separates from the upstream edge of the cavity. When a large-scale vortex collides with the downstream wall, the low-pressure fluid in the vortex spreads along the downstream wall. As a result, a local downward velocity is induced by the local pressure gradient, causing the upstream fluid to expand. Finally, an expansion wave propagates to the outside of the cavity. The large-scale vortices originate from the convective disturbances that develop in the shear layer. The disturbances grow due to the Kelvin–Helmholtz instability, similar to the growth of those in a laminar cavity flow. To clarify the mechanism for the generation of the initial convective disturbances, computations for backward-facing step flows with an artificial acoustic source are also performed. As the artificial acoustic waves become more intense, the initial convective disturbances in the shear layer become more intense while the spatial growth rate of these disturbances does not change. This means that the initial convective disturbances in the shear layer are induced by the acoustic waves. © 2009 American Institute of Physics. [doi:10.1063/1.3253326]

## I. INTRODUCTION

Self-sustained oscillations with fluid-acoustic interactions in a flow over a cavity often radiate intense tonal sound. If unsuppressed, the sound levels in open cavities can reach 160 dB at a freestream Mach number of 0.8.<sup>1</sup> These strong oscillations can cause fatigue in nearby components such as aircraft wheel wells and landing gear compartments. The intense tonal sound radiated by the deep cavity of a train-car gap is a problem to be overcome in the development of faster trains.<sup>2</sup> Large-amplitude pressure pulses can occur in gas transport systems with closed side branches even when the freestream Mach number is lower than 0.2.<sup>3,4</sup> In short, prediction of oscillations during the design stage and invention of ways to suppress them are important in the development of many flow-related industrial products.

Many researchers over the past 50 years have investigated the mechanism of self-sustained oscillations in a cavity flow. Rossiter<sup>5</sup> described an oscillation mechanism similar to that presented for edge tones by Powell.<sup>6</sup> In this mechanism, the interactions of vortices with the downstream edge radiate acoustic waves, which leads to the formation of new vortices at the upstream edge. Rossiter derived a semiempirical formula to explain this:  $fL/u_{1\infty} = (n - \gamma)/(M + 1/\kappa)$ , where  $f$  is the frequency of the radiated tonal sound,  $L$  is the cavity length,  $u_{1\infty}$  is the freestream velocity,  $n$  is a positive integer,  $M$  is the freestream Mach number,  $\kappa$  is the ratio of the convection velocity of the vortices to the freestream velocity,

and  $\gamma$  is a constant for the phase correction. The frequencies predicted by this formula agree with the peak frequencies of the tonal sound measured in his experiments for a cavity flow with an upstream turbulent boundary layer (turbulent cavity flow) at high Mach numbers ( $M > 0.4$ ).<sup>5</sup> East<sup>7</sup> measured pressure fluctuations in a deep cavity with a large depth-to-length ratio ( $D/L > 1$ ) in a turbulent boundary layer at low Mach numbers ( $M < 0.2$ ). He found that intense oscillations occur only when the shear layer instability caused by the fluid-acoustic interactions described by Rossiter<sup>5</sup> is coupled with the acoustic resonance of the cavity.

Rockwell and Naudascher<sup>8</sup> classified the self-sustained oscillations in a cavity flow into two categories. They called oscillations due to shear layer instability without the resonance described by Rossiter<sup>5</sup> “fluid-dynamic oscillations” and those due to the coupling between the shear layer instability and the acoustic resonance of the cavity “fluid-resonant oscillations.” For fluid-dynamic oscillations in a laminar cavity flow, Knisely and Rockwell<sup>9</sup> found by experiments that disturbances generated at the upstream edge by acoustic feedback are amplified in the shear layer by the Kelvin–Helmholtz (KH) instability, resulting in the formation of vortices. On the basis of the feedback loop model described by Rossiter,<sup>5</sup> Rowley *et al.*<sup>10</sup> suggested a criterion for the onset of fluid-dynamic oscillations in a laminar cavity flow, which takes into account the cavity configuration and the freestream Mach number. This criterion agrees with their two-dimensional computational results obtained using the compressible Navier–Stokes equations.<sup>10</sup> They did not discuss oscillations in a turbulent cavity flow. With regard to

<sup>a)</sup>Electronic mail: yokoyama@iis.u-tokyo.ac.jp.

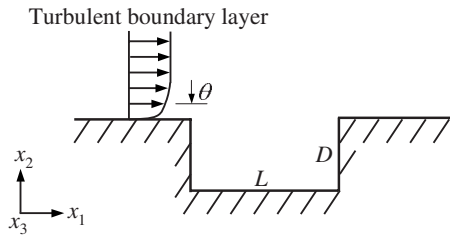


FIG. 1. Configuration for flow over two-dimensional cavity.

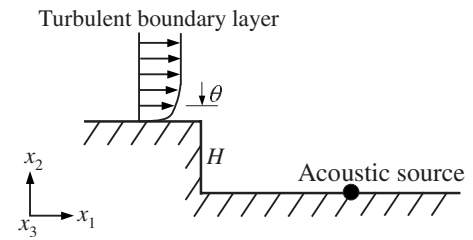


FIG. 2. Configuration for backward-facing step flow.

fluid-resonant oscillations in a turbulent cavity flow, by using particle image velocimetry, Oshkai and Yan<sup>3</sup> showed that large-scale vortices form in the shear layer and that they become acoustic sources. However, the mechanism for the formation of these vortices and that for the acoustic radiation have not been described in detail.

Our objective is to clarify in detail the mechanism for the formation of the large-scale vortices by acoustic feedback and that for the acoustic radiation by these vortices with regard to the self-sustained oscillations of a turbulent cavity flow by directly solving the compressible Navier–Stokes equations. As mentioned, it is important to suppress the oscillations of turbulent cavity flows in various industrial products. In this paper, the fluid-dynamic oscillations are focused on. In a subsequent paper, the fluid-acoustic interactions of fluid-resonant oscillations will be focused on.

## II. NUMERICAL METHODS

### A. Flow configurations

The flow over a two-dimensional cavity, as shown in Fig. 1, is investigated. The incoming boundary layer is turbulent. The parameters are shown in Table I. The freestream Mach number  $M$  is 0.3. The ratio of the momentum thickness to the cavity length  $\theta/L$ , where  $\theta$  is calculated from a separate computation for the flow over a flat plate without a cavity, is 0.04 at the position of the upstream edge of the cavity. The ratio of the momentum thickness of the shear layer to the cavity length  $\theta_m/L$  is 0.06 at  $x_1/L=0.5$ , where the origin of the coordinate is at the position of the upstream edge of the cavity. The momentum thickness is defined as

$$\theta_m = \int_{y_{\min}}^{y_{\max}} \frac{u_{1av}}{u_{1\infty}} \left(1 - \frac{u_{1av}}{u_{1\infty}}\right) dx_2, \quad (1)$$

where  $u_{1av}$  is the time- and spanwise-averaged streamwise velocity. The boundary  $y_{\min}/L=-0.1$  is adopted to remove the effect of the inverse flow in the cavity. Also,  $y_{\max}/L$  is set to 1.0 because the  $u_{1av}/u_{1\infty}$  is approximately 1.0 at this position. The parameters of  $M$  and  $\theta/L$  have the same values as those used by Mizushima *et al.*<sup>2</sup> in their investigation of a

TABLE I. Parameters.

Label	$M$	$D/L$	$Re_L$	$\theta/L$	$\theta_m/L$
Present computation	0.3	0.5	$3.0 \times 10^4$	0.04	0.06
Train-car gap experiment <sup>a</sup>	0.3	0.5–2.6	$6.6 \times 10^5$	0.04	...

<sup>a</sup>Reference 2.

cavity flow. In their experiment, they measured sound radiating from the flow over the cavity of a train-car gap, for which  $D/L$  ranged from 0.5 to 2.6 around the train car, and found that self-sustained oscillations occurred.

Preliminary computations of cavity flow were performed for different values of  $D/L$  (0.5, 0.9, 1.3, 1.7, 2.1, and 2.5) while keeping the cavity length and incoming boundary layer thickness constant. The results showed that fluid-dynamic oscillations occurred when  $D/L$  was 0.5 and that fluid-resonant oscillations occurred when it was  $\geq 0.9$ .

Here the fluid-dynamic oscillations are clarified for a cavity flow when  $D/L$  is 0.5 ( $L/D=2.0$ ,  $\theta/D=0.08$ ). A subsequent paper will focus on the fluid-acoustic interactions of the fluid-resonant oscillations for deep cavities with  $D/L \geq 0.9$ . The Reynolds number  $Re_L$  ( $=\rho_{\infty} u_{1\infty} L / \mu$ , where  $\rho_{\infty}$  and  $\mu$  are, respectively, the density and viscosity of the free stream), is  $3.0 \times 10^4$  in the present computation, whereas it was  $6.6 \times 10^5$  in Mizushima's experiment.<sup>2</sup> The effects of this difference in the Reynolds number on the fluid-acoustic interactions in fundamental oscillations are small, as explained in Sec. III D.

Computations for a backward-facing step (backstep) flow, as shown in Fig. 2, are also performed. In the backstep flow, tonal sound is not radiated by itself. To clarify the mechanism for the formation of large-scale vortices in the shear layer of the cavity flow due to acoustic feedback, the effects of artificial acoustic waves on the shear layer of the backstep flow are investigated. The boundary layer at the trailing edge is the same as that at the upstream edge of the cavity in the cavity flow. The backstep height  $H$  is the same as the cavity depth of  $0.5L$ .

### B. Governing equations and finite difference formulation

Both flow and acoustic fields are simultaneously simulated by directly solving the three-dimensional compressible Navier–Stokes equations in the conserved form

$$\mathbf{Q}_t + \frac{\partial}{\partial x_k} (\mathbf{F}_k - \mathbf{F}_{vk}) = 0, \quad (2)$$

where  $\mathbf{Q}$  is the vector of the conserved variables,  $\mathbf{F}_k$  is the inviscid flux vector, and  $\mathbf{F}_{vk}$  is the viscous flux vector.

The spatial derivatives are evaluated using the sixth-order-accurate compact finite difference scheme (fourth order accurate on the boundaries).<sup>11</sup> The time integration is done using the third-order-accurate Runge–Kutta method.

To reduce the computational cost, large-eddy simulations (LES) are performed in the present work. Nevertheless, the present computational grid incorporated with the above-mentioned numerical methods adequately resolves the smallest active vortices in the boundary layer and in the shear layer in the cavity. To derive the governing equations for LES, any variable  $\psi$  is decomposed into its grid-scale (GS)  $\bar{\psi}$  and subgrid-scale (SGS)  $\psi''$  components,

$$\psi = \bar{\psi} + \psi'' . \quad (3)$$

In a compressible flow, the GS quantity is recast in terms of a Favre-filtered variable

$$\tilde{\psi} = \frac{\overline{\rho\psi}}{\bar{\rho}} . \quad (4)$$

The GS components of the conserved variables and the fluxes are given as

$$\mathbf{Q} = \frac{1}{J} (\bar{\rho}, \bar{\rho}\tilde{u}_1, \bar{\rho}\tilde{u}_2, \bar{\rho}\tilde{u}_3, \bar{\rho}\tilde{e})^t, \quad (5)$$

$$\mathbf{F}_k = \frac{1}{J} \begin{pmatrix} \bar{\rho}\tilde{u}_k \\ \bar{\rho}\tilde{u}_1\tilde{u}_k + \bar{p} \\ \bar{\rho}\tilde{u}_2\tilde{u}_k + \bar{p} \\ \bar{\rho}\tilde{u}_3\tilde{u}_k + \bar{p} \\ (\bar{\rho}\tilde{e} + \bar{p})\tilde{u}_k \end{pmatrix}, \quad (6)$$

$$\mathbf{F}_{vk} = \frac{1}{J} \begin{pmatrix} 0 \\ \tilde{\sigma}_{k1} \\ \tilde{\sigma}_{k2} \\ \tilde{\sigma}_{k3} \\ \tilde{u}_j\tilde{\sigma}_{kj} + \kappa \frac{\partial \tilde{T}}{\partial x_k} \end{pmatrix}, \quad (7)$$

$$\tilde{\sigma}_{kl} = \mu(\tilde{T}) \left( \frac{\partial \tilde{u}_k}{\partial x_l} + \frac{\partial \tilde{u}_l}{\partial x_k} - \frac{2}{3} \delta_{kl} \frac{\partial \tilde{u}_n}{\partial x_n} \right), \quad (8)$$

$$\kappa = \mu(\tilde{T}) C / \text{Pr}, \quad (9)$$

where  $\sigma_{kl}$  is the viscous stress tensor,  $\kappa$  is the thermal conductivity, and  $\delta_{kl}$  is the Kronecker's delta function. The fluid is assumed to be the standard air. Sutherland's formula is used for the viscosity coefficient  $\mu$ . It is assumed that the specific heat  $C$  is  $1004 \text{ J kg}^{-1} \text{ K}^{-1}$  and that the Prandtl number  $\text{Pr}$  is  $0.72$ . No explicit SGS model is used here: the turbulent energy in the GS that should be transferred to SGS eddies is dissipated by the tenth-order spatial filter, as described below. It was shown by many researchers<sup>12-14</sup> that the above-mentioned method combining the low-dissipation discretization schemes and the explicit filtering correctly reproduces turbulent flows such as a cavity flow and a round jet. This filter removes numerical instabilities at the same time,<sup>15</sup>

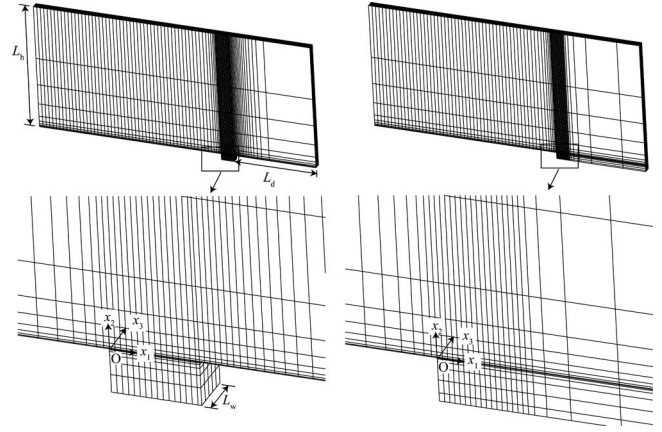


FIG. 3. Computational grids for cavity flow (left) and backward-facing step flow (right). Every tenth grid line is shown for clarity.

$$\alpha_f \hat{\psi}_{i-1} + \hat{\psi}_i + \alpha_f \hat{\psi}_{i+1} = \sum_{n=0}^5 \frac{a_n}{2} (\psi_{i+n} + \psi_{i-n}), \quad (10)$$

where  $\psi$  is a conserved quantity and  $\hat{\psi}$  is the filtered quantity. The coefficients  $a_n$  have the same values as those used by Gaitonde and Visbal,<sup>16</sup> and the parameter  $\alpha_f$  is  $0.45$ . In Sec. III, these computational methods are validated.

### C. Computational grid

Figure 3 shows the computational grids for the cavity and backstep flows. The origins of the coordinates are at the position of the upstream edge of the cavity and that of the trailing edge of the backstep, respectively. The spanwise extents of these computational domains  $L_w$  are  $0.5L$  and  $H$  for the cavity and backstep flows, respectively. This extent corresponds to  $L_w^+ = 700$ , where the wall units are based on the skin-friction coefficient computed for the boundary layer over a flat plate at the streamwise position corresponding to the upstream edge of the cavity and the trailing edge of the backstep,  $\text{Re}_x = 4.3 \times 10^5$ . Therefore, approximately six turbulent streaks lie in the spanwise extent. The cross sections in the  $x_1$ - $x_2$  plane are shown in Fig. 4, where length is non-dimensionalized by cavity length  $L$  and backstep height  $H$  for the cavity and backstep flows, respectively. The effects of the extent of the computational domain on the results are discussed in Sec. III C.

To capture the longitudinal vortices in the turbulent boundary layer, the grid resolutions are set near the wall as  $\Delta x_1^+ = 38$ ,  $\Delta x_2^+ = 1$ , and  $\Delta x_3^+ = 14$ , where the wall units are based on the above-mentioned skin-friction coefficient. To capture the acoustic propagation accurately, more than 20 grid points are used per acoustic wavelength of the fundamental frequency of the oscillations even in the field far from the cavity. It is clarified in Sec. III that the present computational grid adequately resolves both the longitudinal vortices in the turbulent boundary layer and the acoustic waves created by the fundamental oscillations. The present computational domain consists of approximately  $5.0 \times 10^6$  structured grid points.

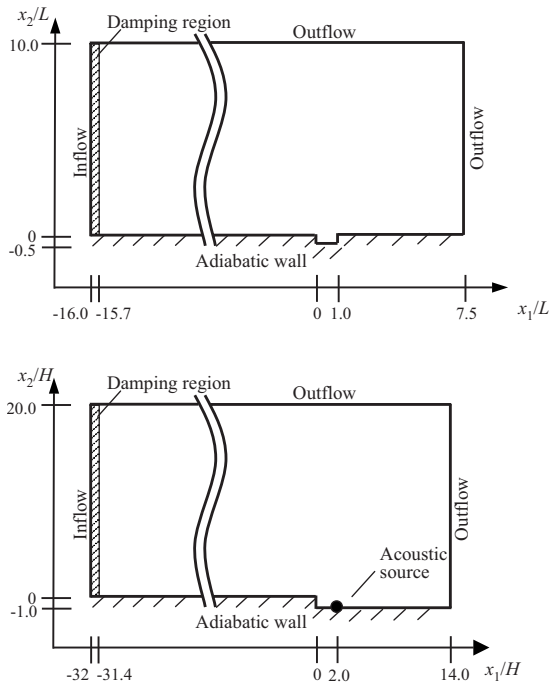


FIG. 4. Computational domains and boundary conditions for cavity flow (top) and backward-facing step flow (bottom).

#### D. Boundary conditions

Figure 4 also shows the boundary conditions for the cavity and backstep flows. The inflow and outflow boundaries are artificial, so that they must allow vortices and acoustic waves to pass smoothly with minimal numerical disturbances. Nonreflecting boundary conditions based on the characteristic wave relations<sup>17–19</sup> are used at these boundaries. Nonslip and adiabatic boundary conditions are used at the wall. The periodic boundary condition is used in the spanwise ( $x_3$ ) direction. The use of the periodic condition is appropriate in the present study because the disturbances in the shear layer two dimensionally grow to large-scale vortices due to the KH instability and radiate two-dimensional acoustic waves in the fundamental oscillations, as explained in Sec. IV.

To achieve the desired momentum thickness of the boundary layer at the upstream edge of the cavity, Eq. (2) is replaced with

$$\mathbf{Q}_t + \frac{\partial}{\partial x_k} (\mathbf{F}_k - \mathbf{F}_{vk}) = -\sigma_0 (a/L_d) x_d^2 (\mathbf{Q} - \mathbf{Q}_{\text{target}}) \quad (11)$$

for the upstream damping region shown in Fig. 4, where  $a$  is the speed of sound,  $L_d$  is the streamwise length of the damping region,  $x_d$  is the nondimensional distance from the downstream end of the damping region ( $0 \leq x_d \leq 1$ ), and  $\mathbf{Q}_{\text{target}}$  is the target vector of the conserved variables.<sup>20,21</sup> The coefficient  $\sigma_0$  is set to 0.05. It was demonstrated in a previous study that acoustic reflection does not occur with this setting.<sup>22</sup> At the inflow boundary of the computational domain, the Reynolds number  $\text{Re}_x$  ( $=\rho_\infty u_{1\infty} x / \mu$ , where  $x$  is the distance measured from the origin of the laminar boundary layer) and boundary layer thickness  $\delta_{\text{int}}/L$  are assumed to be  $9.0 \times 10^3$  and 0.016, respectively.

Laminar-turbulent transition is prompted by superimposing homogeneous freestream turbulence on the solutions for the compressible laminar boundary layer  $\mathbf{Q}_{\text{Blasius}}$  for  $1.25 < x_2/\delta_{\text{int}} < 21.3$  ( $0.02 < x_2/L < 0.34$ ) in the damping region ( $-16.0 < x_1/L < -15.7$ ), where  $x_2=0$  corresponds to the position of the wall. That is,

$$\mathbf{Q}_{\text{target}} = \mathbf{Q}_{\text{Blasius}}(x_2/\delta_{\text{int}} \leq 1.25, 21.3 \leq x_2/\delta_{\text{int}}), \quad (12)$$

$$\mathbf{Q}_{\text{target}}(t) = \mathbf{Q}_{\text{Blasius}} + \mathbf{Q}_{\text{fst}}(t) (1.25 < x_2/\delta_{\text{int}} < 21.3).$$

The freestream turbulence  $\mathbf{Q}_{\text{fst}}(t)$  is obtained by sliding an instantaneous frozen flow field of homogeneous turbulence computed by a separate LES. In the simulation of the homogeneous turbulence, the initial random field has the Karman spectrum.<sup>23</sup> The turbulence intensity is 6%, and the longitudinal integral scale is about  $0.24L$ . This integral scale corresponds to about  $0.06\lambda$ , where  $\lambda$  is the acoustic wavelength of the fundamental frequency of the sound radiating from the cavity flow, and the effect of the freestream turbulence on the propagation of the radiated acoustic waves is negligibly small. Also, it was confirmed that the amplitude of the spurious noise generated by the superimposition of this freestream turbulence is less than 10% of that of the sound generated by the oscillations on the bottom of the cavity, where we observe the pressure fluctuations in Sec. IV B. Therefore, it is concluded that the effects of the freestream turbulence on the oscillations of the cavity flow are also small. It is demonstrated in Sec. III B that the boundary layer becomes a fully developed turbulent state by the upstream edge of the cavity.

#### E. Initial flow fields

The computational result for the turbulent flow over a flat plate is used as the initial flow field for the present computation of the turbulent cavity flow. In the cavity region ( $0 \leq x_1 \leq L$  and  $x_2 < 0$ ), the velocity is set to 0, and the pressure and density are set to the same values as those at  $x_2=0$ .

### III. VALIDATION OF COMPUTATIONAL METHODS

#### A. Propagation of acoustic waves

The effects of the grid resolution on the propagation of acoustic waves were preliminarily investigated by using an artificial monopole. As a result, it was clarified that five grid points per one wavelength accurately capture the acoustic waves. Therefore, the present computational grids for the main computations, for which more than 20 grid points are used per one acoustic wavelength, sufficiently resolve the propagation of the acoustic waves for the fundamental oscillations.

#### B. Turbulent boundary layer

To confirm that the boundary layer has become a fully developed turbulent state by the upstream edge of the cavity, the flow over a flat plate with a cavity is calculated. Figure 5 shows the variation in the computed time- and spanwise-averaged skin-friction coefficient  $c_f$  compared with

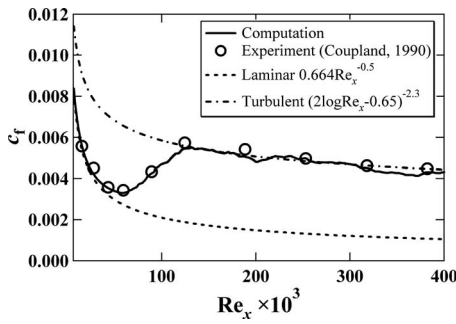


FIG. 5. Variations in time- and spanwise-averaged skin-friction coefficients computed for flat plate boundary layer without cavity.

that measured in the past experiment<sup>24</sup> with the same degree of freestream turbulence intensity as that of the present computation. The computed skin-friction coefficients are in good agreement with those measured in the experiment.<sup>24</sup> The boundary layer becomes a fully developed turbulent state at  $Re_x = 4.3 \times 10^5$ , where the upstream edge of the cavity is to be located for the main computations.

For the main computation of the cavity flow, the spanwise cross-correlation coefficient  $R$  of  $u_2$  along  $x_2^+ = 15$  at the upstream position of the cavity  $Re_x = 3.4 \times 10^5$  is shown in Fig. 6. The spanwise extent of the computational domain  $L_w^+$  corresponds to 720. This coefficient is computed from the flow fields sampled during  $T^+ = 300$  using Eq. (13). The spanwise periodicity is used when  $x_3 + \Delta x_3$  is larger than  $L_w$ ,

$$R(\Delta x_3) = \frac{\int_{t=0}^{T^+=300} \int_{x_3=0}^{x_3=L_w} u_2'(x_3) u_2'(x_3 + \Delta x_3) dx_3 dt}{\int_{t=0}^{T^+=300} \int_{x_3=0}^{x_3=L_w} u_2'(x_3) u_2'(x_3) dx_3 dt}, \quad (13)$$

where  $u_2'$  is the difference between the instantaneous and time-averaged velocity components in the  $x_2$  direction. In Fig. 6, the local minimum of the coefficient, which appears at around  $\Delta x_3^+ = 60$ , shows that the mean spanwise streak spacing is about 120. This value is in good agreement with that presented in the past research.<sup>25</sup> This indicates that the longitudinal vortices, which generate the streaks in the turbulent boundary layer, are adequately captured in the present computation.

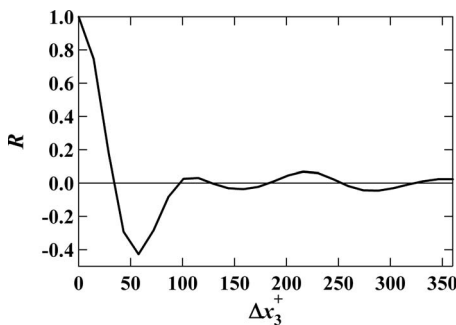


FIG. 6. Spanwise cross-correlation coefficient of vertical velocity  $u_2$  along  $x_2^+ = 15$  at  $Re_x = 3.4 \times 10^5$  for cavity flow.

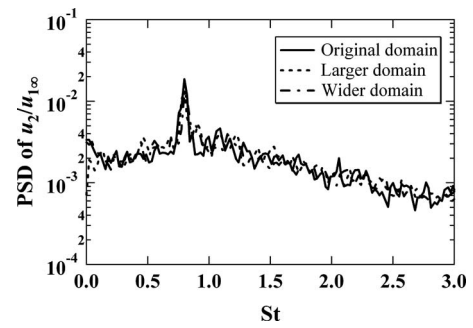


FIG. 7. Power spectral densities of vertical velocity  $u_2/u_{1\infty}$  at  $x_1/L = 0.5$  and  $x_2 = 0$  for cavity flow with original computational domain ( $L_h/L = 10.0$ ,  $L_d/L = 6.5$ ,  $L_w/L = 0.5$ ), with larger domain ( $L_h/L = 15.0$ ,  $L_d/L = 9.7$ ,  $L_w/L = 0.5$ ), and with wider domain ( $L_h/L = 10.0$ ,  $L_d/L = 6.5$ ,  $L_w/L = 1.0$ ).

### C. Effects of computational domain

It is of critical importance that the computational domain does not affect the results. To confirm that it does not, two additional computations for the cavity flow with computational domains different from the original domain are also performed.

First, the effects of the vertical length  $L_h$  and the streamwise length  $L_d$  from the downstream edge of the cavity to the downstream outflow boundary are investigated. The calculations with a domain ( $L_h/L = 15.0$ ,  $L_d/L = 9.7$ ,  $L_w/L = 0.5$ ) larger than the original domain ( $L_h/L = 10.0$ ,  $L_d/L = 6.5$ ,  $L_w/L = 0.5$ ) are performed. Then, the effects of the spanwise length  $L_w$  are investigated by performing the calculation for a cavity flow with a domain with a twice-extended spanwise length ( $L_h/L = 10.0$ ,  $L_d/L = 6.5$ ,  $L_w/L = 1.0$ ). The grid resolutions of the two extended computational domains are the same as that of the original computational domain for the corresponding regions.

Figure 7 compares for these three domains the frequency spectra of the velocity fluctuations at  $x_1/L = 0.5$  and  $x_2 = 0$ . Frequency  $f$  is normalized as  $St \equiv fL/u_{1\infty}$ . The duration of the Fourier transform is about  $45(L/u_{1\infty})$ , and the results are averaged 20 times temporally as well as spanwisely. This duration corresponds to about 36 periods of the fundamental mode  $St = 0.8$  for the cavity flow. Figure 7 shows that both the frequency and the amplitude of the fundamental oscillations with the two extended domains are virtually identical to those with the original domain. Therefore, it is concluded that the original computational domain is sufficiently large and wide and does not affect the present results.

### D. Comparison to experiments

As shown in Table I, the flow parameters in the present computation have the same values as those in Mizushima's experiment<sup>2</sup> except for the cavity depth and the Reynolds number. In the experiment,  $D/L$  varied from 0.5 to 2.6. The fundamental frequency  $St = 0.8$  in the present computation for the cavity flow closely agrees with that measured in the experiment ( $St = 0.78$ ), while oscillations at  $St = 0.4$  also occurred in the experiment. Preliminarily, it was demonstrated that the oscillations at  $St = 0.4$  occur for a cavity flow with

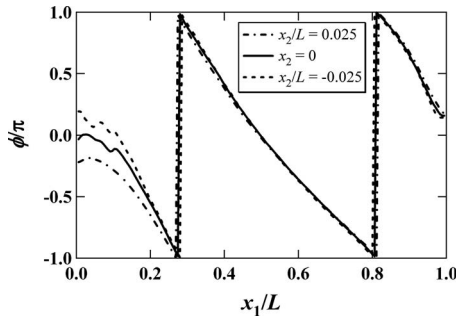


FIG. 8. Spatial distributions of the phase in velocity  $u_2$  along  $x_2/L=0.025$ , 0, and  $-0.025$ .

$D/L=1.3$  and that they correspond to the fluid-resonant oscillations. The fluid-acoustic interactions of the fluid-resonant oscillations will be investigated in a subsequent paper. Meanwhile, the mode at  $St=0.8$  corresponds to the fluid-dynamic oscillations, which are the primary focus of this paper.

As mentioned, the effect of the difference in the Reynolds number  $Re_L$  between the present computation and Mizushima's experiment<sup>2</sup> on the fluid-acoustic interactions in the fundamental oscillations is presumably small for the following reason. Namely, in the present computation for the cavity flow, the two-dimensional disturbances in the shear layer grow to large-scale vortices due to the KH instability of the inflection point of the averaged velocity profile, as clarified in Sec. IV. This indicates that the interactions between the large-scale vortices and the turbulent fine-scale vortices are small, and therefore the fluid-acoustic interactions in the fundamental oscillations do not strongly depend on the Reynolds number. Hence it can be mentioned that the present computation captures the fluid-acoustic interactions in the fluid-dynamic oscillations observed in the experiment.

## IV. RESULTS AND DISCUSSION

### A. Analysis methods

#### 1. Spatial variations in power spectral density and phase

The spatial variations in the power spectral density (PSD) and the phases of the variables are computed from the results of the Fourier transform of spanwise-averaged data. The duration of the Fourier transform is  $10(L/u_{1\infty})$ , which corresponds to eight periods of the fundamental frequency for the cavity flow. The variations are averaged 20 times temporally.

#### 2. Linear stability analysis

Linear stability analysis (LSA) is performed in a standard way<sup>10,26,27</sup> and thus is described only briefly here. A compressible, inviscid, locally parallel formulation is used. This means that the time-averaged velocity profile slowly varies in the streamwise direction and that the disturbances are parallel at each streamwise location. To confirm that the disturbances for the fundamental frequency are parallel in the shear layer of the cavity flow, we investigated the spatial distributions of the phase of velocity  $u_2$  for the fundamental

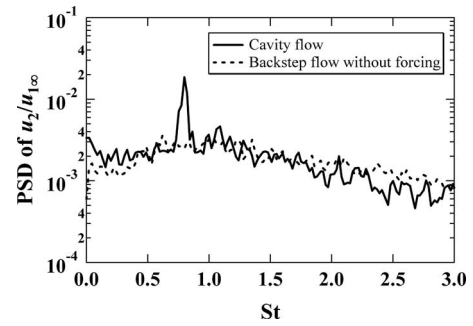


FIG. 9. PSD of vertical velocity  $u_2/u_{1\infty}$  at  $x_1/L=0.5$  and  $x_2/L=0$  for cavity flow and at  $x_1/H=1.0$  and  $x_2/H=0$  for backward-facing step flow.

frequency along  $x_2/L=0.025$ , 0, and  $-0.025$ , as shown in Fig. 8, where the reference of the phases is the phase at  $x_1/L=0.5$  and  $x_2/L=0$ . As a result, it was clarified that the three phase distributions approximately agree with each other and therefore, the disturbances are parallel. The slight difference near the upstream edge is due to the effects of the particle velocity of the acoustic waves on the velocity  $u_2$ . Also, the normal modes of the form

$$g(x_1, x_2, t) = \hat{g}(x_2)e^{i(\alpha x_1 + 2\pi ft)} + \text{c.c.} \quad (14)$$

are assumed, where  $f$  is a frequency,  $\alpha$  is a complex eigenvalue,  $g$  is any flow variable,  $\hat{g}$  is a complex eigenfunction, and c.c. denotes the complex conjugate. The modes are inserted into the compressible inviscid equations linearized about the parallel flow, and the eigenvalues and eigenfunctions are found using a Runge–Kutta shooting method. The present LES data are used to determine the mean flow for the LSA. Boundary conditions are set such that the disturbances are exponentially dampened for large  $+x_2$ , and zero vertical velocity is imposed at the bottom wall of the cavity.

### 3. Spanwise cross correlation

The spanwise cross-correlation coefficient  $R_f$  of  $u_2$  for the fundamental frequency is computed using Eq. (15). The spanwise periodicity is used when  $x_3 + \Delta x_3$  is larger than  $L_w$ ,

$$R_f(\Delta x_3) = \frac{\int_{t=0}^{t=20T} \int_{x_3=0}^{x_3=L_w} u_{2f}(x_3) u_{2f}(x_3 + \Delta x_3) dx_3 dt}{\int_{t=0}^{t=20T} \int_{x_3=0}^{x_3=L_w} u_{2f}(x_3) u_{2f}(x_3) dx_3 dt}, \quad (15)$$

where  $u_{2f}$  is the velocity fluctuation for the fundamental frequency and computed using the Fourier transform. The duration of the transform is  $10(L/u_{1\infty})$ . This coefficient  $R_f$  represents the two dimensionality of the flow for the fundamental frequency.

### 4. Phase-averaging process

In a phase-averaging process, the variables at the same phase of the fundamental mode are averaged 45 times temporally for the cavity flow. It has been preliminarily clarified by using a wavelet analysis that the period of the oscillations varies by about 5% temporally. Considering this variation in the period, the pressure fluctuation on the bottom

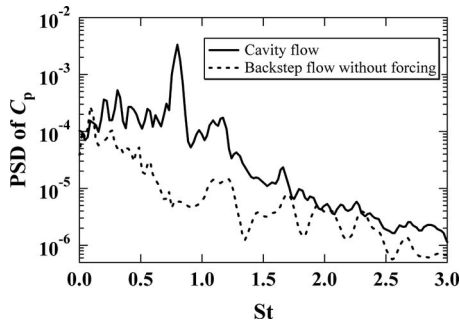


FIG. 10. PSD of pressure coefficient  $C_p$  at  $x_1/L=0.5$  and  $x_2/L=-0.5$  for cavity flow and at  $x_1/H=1.0$  and  $x_2/H=-1.0$  for backward-facing step flow.

( $x_1/L=0.5$ ,  $x_2/L=-0.5$ ) is used as the reference signal. The phase at each time is calculated assuming that the period of the oscillations is the time interval from a peak to a next peak of this pressure fluctuation. The phase-averaged data are further averaged in the spanwise direction.

## B. Self-sustained oscillations

Figure 9 shows the frequency spectrum of the velocity  $u_2$  in the shear layer at  $x_1/L=0.5$  and  $x_2=0$  for the cavity flow and that at the corresponding position for the backstep flow without an artificial acoustic source. Frequency  $f$  is normalized as  $St \equiv 2fH/u_{1\infty}$  for the backstep flow, where  $2H$  corresponds to cavity length  $L$ . Self-sustained oscillations occur at  $St=0.8$  in the cavity flow while oscillations do not occur in the backstep flow. Note also that the amplitudes of the fluctuations at other frequencies for the cavity flow are approximately the same as those for the backstep flow. This means that the self-sustained oscillations do not strongly affect the amplitude of the turbulent kinetic energy at other frequencies in the shear layer.

Figure 10 shows the frequency spectrum of the pressure fluctuations on the bottom wall at  $x_1/L=0.5$  and  $x_2/L=-0.5$  for the cavity flow and that at  $x_1/H=1.0$  and  $x_2/H=-1.0$  for the backstep flow. The pressure is normalized as pressure coefficient  $C_p \equiv p/(\rho_\infty u_{1\infty}^2/2)$ . Tonal sound is radiated in the self-sustained oscillations at  $St=0.8$  only for the cavity flow.

## C. Vortices

### 1. Fine-scale vortices

Instantaneous vortices for the cavity flow are illustrated in Fig. 11. To elucidate the vortices, the second invariant of the velocity gradient tensor  $q = \|\Omega\|^2 - \|S\|^2$  is computed, where  $\Omega$  and  $S$  are, respectively, the asymmetric and symmetric parts of the velocity gradient tensor. Regions with  $q > 0$  represent vortex tubes. Before the separation at the upstream edge, fine-scale longitudinal vortices are active in the turbulent boundary layer. Soon after the separation, these vortices become free from the blocking effect of the wall and become more active than those in the upstream turbulent boundary layer.

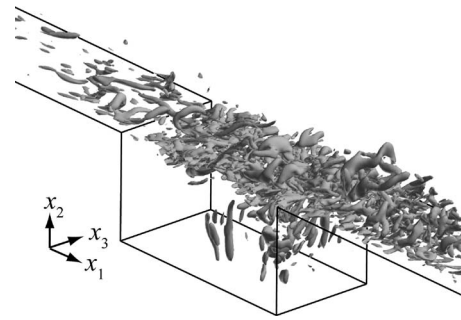


FIG. 11. Instantaneous isosurfaces of  $q/(u_{1\infty}/L)^2=25$  for cavity flow.

### 2. Large-scale vortices

In Fig. 12, the contours and vectors represent the phase-averaged pressure coefficients and velocity vectors, respectively, with the time-averaged components at each position subtracted. Large-scale vortices are apparent in the shear layer and form low-pressure regions. These large-scale vortices are composed of the above-mentioned fine-scale vortices.

Figure 13 shows the spanwise cross-correlation coefficients  $R_f$  of  $u_2$  for the fundamental frequency along  $x_1/L=0.25$ ,  $0.50$ , and  $0.75$  ( $x_2=0$ ) for the cavity flow. The coefficients are high at all positions, which means that the large-scale vortices are coherent in the spanwise direction.

These large-scale vortices form by the growth of the convective disturbances in the shear layer. In Sec. IV E, it will be clarified that the acoustic waves only generate the initial convective disturbances and it does not contribute to the growth of these disturbances. To clarify the mechanism of the growth of these convective disturbances, the rate of the streamwise amplification of the fluctuations in  $u_2$  for the fundamental frequency is compared with that predicted by the LSA in Fig. 14. Note that velocity  $u_2$  includes a convective component and a propagative component (particle velocity). As will be clarified in Sec. IV E, the propagative distur-

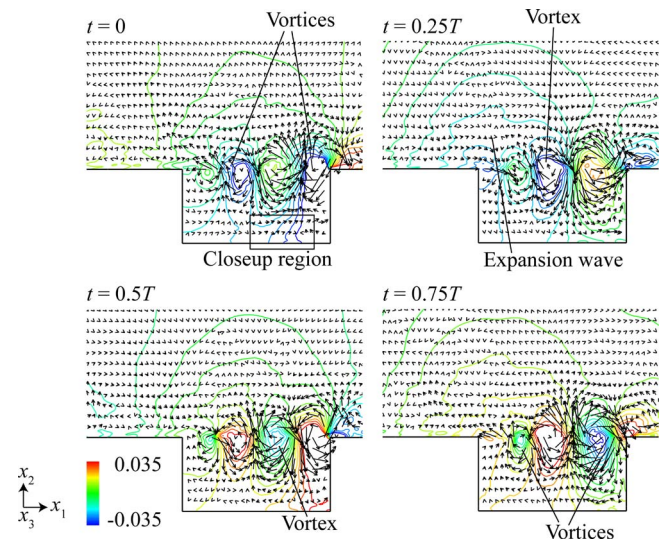


FIG. 12. (Color online) Phase-averaged pressure coefficients and velocity vectors for cavity flow, where  $T$  is the time period of fundamental oscillations.

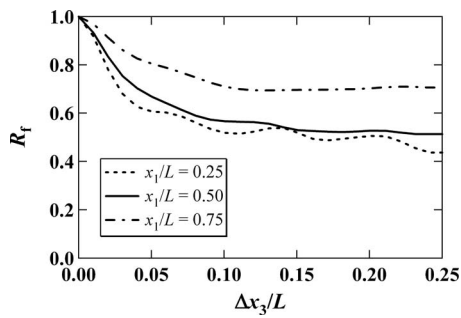


FIG. 13. Spanwise cross-correlation coefficient  $R_f$  of vertical velocity  $u_2$  for fundamental frequency along  $x_1/L=0.25, 0.50,$  and  $0.75$  ( $x_2=0$ ) for cavity flow.

bances of the acoustic waves are negligible in comparison to the convective disturbances in the shear layer of  $x_1 > 0.1L$ . Therefore, this region is focused on. The amplification rate computed from the present LES data approximately agrees with that predicted by the LSA although at around  $x_1/L=0.2$  the rate becomes gradually saturated as the average velocity gradient becomes more moderate. This means that the convective disturbances of the fundamental frequency in the shear layer grow into large-scale vortices due to the KH instability, similar to those in a laminar cavity flow.<sup>9,10</sup> Meanwhile, the mechanism of the generation of the convective disturbances near the upstream edge ( $x_1 < 0.1L$ ) is not clear because the propagative disturbances of the acoustic waves are comparable to the convective disturbances near the upstream edge. In Sec. IV E, the mechanism of the generation of the initial convective disturbances by the acoustic feedback is discussed by decomposing the flow field into the convective and propagative components for the backstep flow with an artificial acoustic source.

#### D. Acoustic radiation mechanism

The contours in Fig. 15 represent the phase-averaged pressure coefficients with the time-averaged components subtracted. Figure 15 shows that an acoustic wave is radiated from the cavity and propagates to the outside of the cavity.

As already mentioned with relation to Fig. 12, large-scale vortices are apparent in the shear layer. Low-pressure regions are formed in these large-scale vortices. When the large-scale vortices are being convected in the shear layer, the pressure gradient balances with the centrifugal force act-

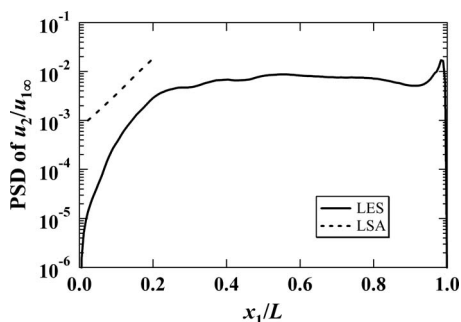


FIG. 14. Growth of PSD of vertical velocity  $u_2/u_{1\infty}$  along  $x_2=0$  for cavity flow compared with that predicted by LSA.

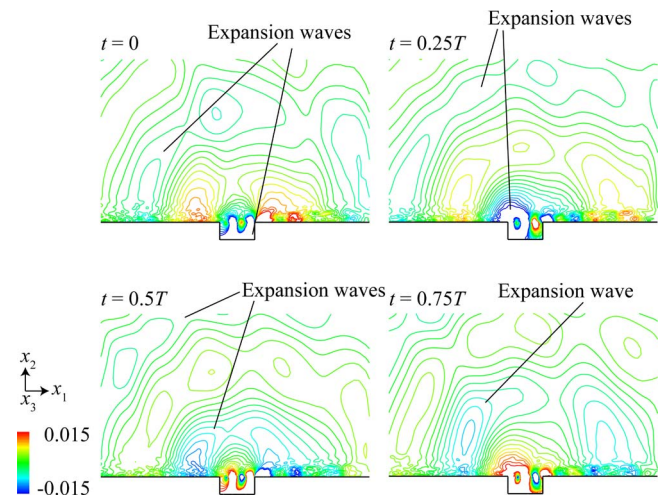


FIG. 15. (Color online) Phase-averaged pressure coefficients for cavity flow, where  $T$  is the time period of fundamental oscillations.

ing on the rotating fluid in the large-scale vortices. However, when a large-scale vortex collides with the downstream wall of the cavity, it is distorted and the low-pressure fluid in the vortex spreads along the downstream wall, as shown in Fig. 12 ( $t=0$ ). At this time, the low-pressure fluid is not rigidly rotating, in contrast to the fluid in the large-scale vortices being convected in the shear layer. This means that the local pressure gradient no longer balances with the centrifugal force. As a result, a local downward velocity is induced due to the local pressure gradient, as shown in Fig. 16, where the detailed phase-averaged flow field is presented at  $t=0$  in Fig. 12. As shown in Fig. 16, this local downward velocity is weak in the far upstream region, while it is intense near the downstream wall. Therefore, the fluid in the upstream region of the downstream wall expands, an expansion wave is radiated, and finally the radiated expansion wave is propagated to the outside of the cavity. To the best of the authors' knowledge, this is the first time that the mechanism of the acoustic radiation is clarified for the cavity flow in detail.

To roughly estimate the position of the acoustic source for the cavity flow, we compute the acoustic propagation from an artificial source placed on the downstream wall without a free stream, as shown in Fig. 17. Also, as shown later in Sec. IV E 3, the effects of the mean flow on the acoustic propagation are negligibly small at the present Mach number of 0.3. The acoustic source is assumed to be two dimensional and coherent in the  $x_3$  (spanwise) direction.

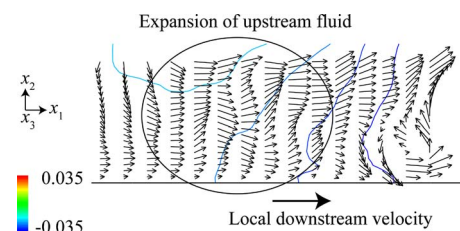


FIG. 16. (Color online) Phase-averaged pressure coefficients and velocity vectors near the bottom wall for cavity flow at  $t=0$  in Fig. 12 (the region in this figure is indicated in Fig. 12).

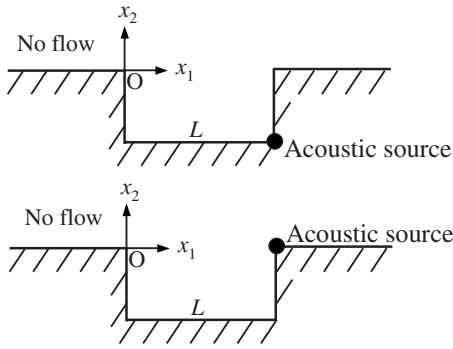


FIG. 17. Flow configurations for acoustic propagation from artificial source without free stream.

The acoustic source is located at two different positions of  $(x_{1a}/L, x_{2a}/L)$ ,  $(1.0, -0.5)$  and  $(1.0, 0)$ , and both the results are compared with the result of the cavity flow for  $M=0.3$ . For doing so, Eq. (1) is replaced with Eqs. (16)–(18) in the regions  $(0.8 < x_1/L < 1.0, -0.5 < x_2/L < -0.3)$  and  $(0.8 < x_1/L < 1.0, -0.2 < x_2/L < 0.2)$ ,<sup>28</sup>

$$\mathbf{Q}_t + \frac{\partial}{\partial x_k} (\mathbf{F}_k - \mathbf{F}_{vk}) = \mathbf{S}, \quad (16)$$

$$\mathbf{S} = \begin{pmatrix} S \\ 0 \\ 0 \\ 0 \\ \left(\frac{5}{2}a^2\right)S \end{pmatrix}, \quad (17)$$

$$S = A \exp \left[ -\ln 2.0 \left( \frac{(x_1 - x_{1a})^2 + (x_2 - x_{2a})^2}{(0.1L)^2} \right) \right] \sin 2\pi ft, \quad (18)$$

where  $A/\rho_\infty$  is  $3.0 \times 10^{-5}$ , and the frequency  $f$  is the same as the fundamental frequency for the cavity flow. The amplitude of the pressure fluctuations on the bottom wall at  $x_1/L=0.5$  and  $x_2/L=-0.5$  is approximately the same as that for the cavity flow for  $M=0.3$ . The spatial variations in the phase of the pressure on the bottom wall ( $x_2/L=-0.5$ ) and on the upstream wall ( $x_1=0$ ) are shown in Figs. 18 and 19, respectively. Both the spatial variations in the phase for the artificial acoustic source at  $(x_{1a}/L, x_{2a}/L)=(1.0, -0.5)$  without a free stream are in good agreement with the present computational results for  $M=0.3$ . However, Fig. 18 shows that the slope of the pressure phase for the artificial acoustic source at  $(x_{1a}/L, x_{2a}/L)=(1.0, 0)$  is different near the downstream wall ( $x_1/L=1.0$ ) from that of the cavity flow for  $M=0.3$ . This means the acoustic waves are radiated from  $(x_1/L, x_2/L)=(1.0, -0.5)$  rather than  $(x_1/L, x_2/L)=(1.0, 0)$  in the cavity flow. However, it should also be mentioned that the acoustic source in the cavity flow is more complex than a monopole source. Therefore, we only roughly estimate the position of the acoustic source here.

The slope of the phase in Fig. 18 shows that the acoustic waves radiated around the downstream wall ( $x_1/L=1.0$ )

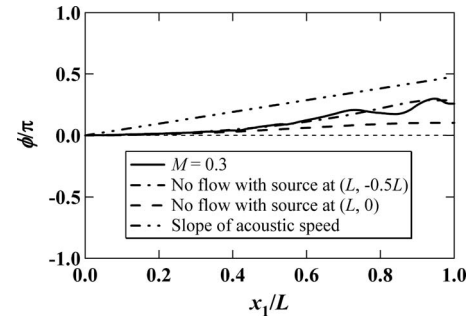


FIG. 18. Phase variations in pressure on bottom ( $x_2=-0.5L$ ) for fundamental frequency for cavity flow of  $M=0.3$  and for two acoustic fields from artificial acoustic source around  $x_1/L=1.0$  and  $x_2/L=-0.5$  and around  $x_1/L=1.0$  and  $x_2/L=0$  without a free stream.

are propagated in the upstream direction ( $-x_1$ ) to about  $x_1/L=0.4$  at the sound speed. However, the slope of the phase becomes approximately flat near the upstream wall ( $x_1=0$ ). This means that the propagation direction of the acoustic waves changes from the  $-x_1$  direction to the  $+x_2$  direction near the upstream wall. The slope of the phase in Fig. 19 shows that the acoustic waves are propagated in the  $+x_2$  direction along the upstream wall at the sound speed.

## E. Backward-facing step flow with artificial acoustic source

### 1. Artificial acoustic source

To clarify the mechanism for the generation of the initial convective disturbances in the shear layer of the cavity flow by the acoustic feedback, the effects of artificial acoustic waves on the shear layer of a backstep flow are also investigated. As shown in Fig. 4, the artificial acoustic source is placed at  $(x_{1a}/H, x_{2a}/H)=(2.0, -1.0)$ , where the backstep height  $H$  corresponds to  $0.5L$  for the cavity flow. This position corresponds to the position of the acoustic source of the cavity (the bottom of the downstream wall), which was roughly estimated in Sec IV D. The acoustic source is added

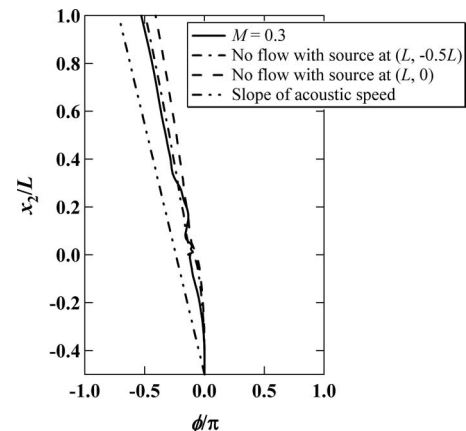


FIG. 19. Phase variations in pressure on upstream wall ( $x_1=0$ ) for fundamental frequency for cavity flow of  $M=0.3$  and for two acoustic fields from artificial acoustic source around  $x_1/L=1.0$  and  $x_2/L=-0.5$  and around  $x_1/L=1.0$  and  $x_2/L=0$  without a free stream.

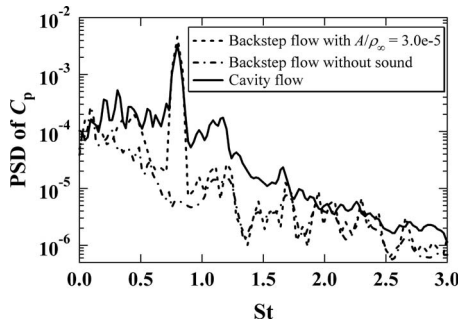


FIG. 20. PSD of pressure coefficient  $C_p$  at  $x_1/H=1.0$  and  $x_2/H=-1.0$  for backward-facing step flows with and without artificial acoustic source and at  $x_1/L=0.5$  and  $x_2/L=-0.5$  for cavity flow.

into the backstep flow by replacing Eq. (1) in the regions  $1.6 < x_1/H < 2.4$  and  $-1.0 < x_2/H < -0.6$  with Eqs. (16), (17), and (19),<sup>28</sup>

$$S = A \exp \left[ (-\ln 2.0) \left( \frac{(x_1 - 2H)^2 + (x_2 + H)^2}{(0.2H)^2} \right) \right] \sin 2\pi ft, \quad (19)$$

where  $A$  is the amplitude of the density fluctuations at the streamwise center of the acoustic source. In order to clarify the effects of the intensity of the acoustic waves on the acoustic feedback, three computations with  $A/\rho_\infty = 0$ ,  $1.0 \times 10^{-5}$ , and  $3.0 \times 10^{-5}$  are performed, among which the amplitude of the pressure fluctuations with  $A/\rho_\infty = 3.0e-5$  on the bottom wall at  $x_1/H=1.0$  and  $x_2/H=-1.0$  is approximately the same as that at the corresponding position for the cavity flow. The excitation frequency  $f$  is the same as the fundamental frequency for the cavity flow.

## 2. Comparison to cavity flow

Figure 20 shows the frequency spectra of the pressure fluctuations at  $x_1/H=1.0$  and  $x_2/H=-1.0$  for the backstep flows with and without the artificial sound of  $A/\rho_\infty = 3.0 \times 10^{-5}$  and the pressure fluctuation at the corresponding position for the cavity flow. It is confirmed that the amplitude of the artificial sound of  $A/\rho_\infty = 3.0 \times 10^{-5}$  is approximately the same as that of the tonal sound in the cavity flow. Also,

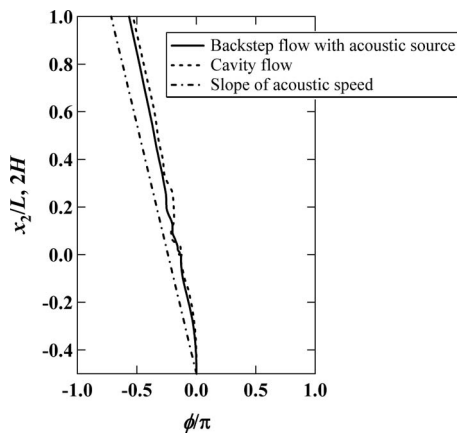


FIG. 21. Phase variations in pressure along  $x_1=0$  for backward-facing step flow with artificial acoustic source and cavity flow.

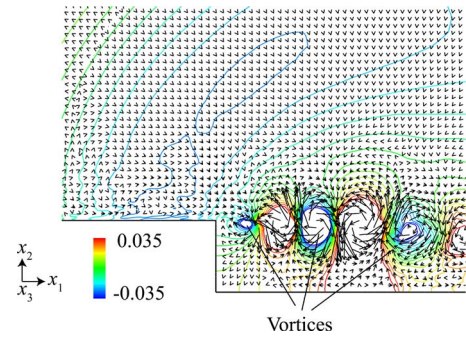


FIG. 22. (Color online) Phase-averaged pressure coefficients and velocity vectors for backward-facing step flow with artificial acoustic source.

the spatial variation in the phase of pressure on the vertical wall ( $x_1=0$ ) for the excitation frequency for the backstep flow with the acoustic source of  $A/\rho_\infty = 3.0 \times 10^{-5}$  is compared with the corresponding variation for the cavity flow in Fig. 21. Figure 21 shows that the spatial variation in pressure phase is also in good agreement with that for the cavity flow. Therefore, it is concluded that the acoustic field in the cavity flow is reproduced in the backstep flow with the artificial acoustic source of  $A/\rho_\infty = 3.0 \times 10^{-5}$ .

In Fig. 22, the contours and vectors represent the phase-averaged pressure coefficients and velocities, respectively, for the backstep flow with the artificial acoustic source of  $A/\rho_\infty = 3.0 \times 10^{-5}$ . By adding the artificial acoustic source, large-scale vortices become apparent in the shear layer and form low-pressure regions like in the cavity flow (Fig. 12).

In Fig. 23, the spanwise cross-correlation coefficients  $R_f$  of  $u_2$  for the excitation frequency along  $x_1/H=0.5$  and  $x_2=0$  for the backstep flow with and without the artificial acoustic source of  $A/\rho_\infty = 3.0 \times 10^{-5}$  are compared with the corresponding coefficient for the cavity flow. The cross-correlation coefficient becomes as high as 0.9 for the backstep flow with the artificial acoustic source, although it is almost zero if the artificial acoustic source is not added. This is because the above-mentioned large-scale vortices are coherent in the spanwise direction like in the cavity flow. Note also that the cross-correlation coefficient for the backstep flow with the artificial acoustic source of  $A/\rho_\infty = 3.0 \times 10^{-5}$  is higher than that for the cavity flow. This is because the artificial acoustic source is perfectly coherent in the spanwise

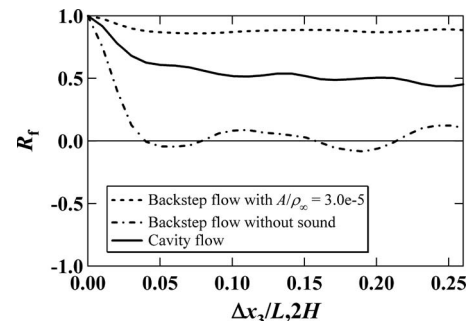


FIG. 23. Spanwise cross-correlation coefficients  $R_f$  of vertical velocity  $u_2$  along  $x_1/H=0.5$  and  $x_2=0$  for backward-facing step flows with and without artificial acoustic source and that along the corresponding line for cavity flow.

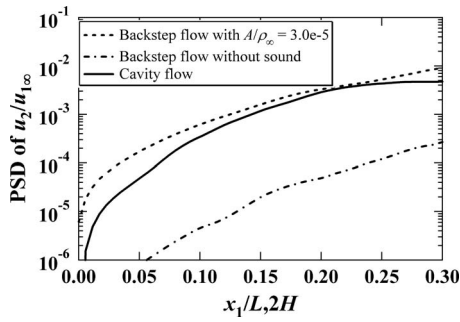


FIG. 24. Variations in PSD of vertical velocity  $u_2/u_{1\infty}$  along  $x_2=0$  for backward-facing step flows with and without artificial acoustic source compared with that for cavity flow.

direction while the large-scale vortices, which become the acoustic sources for the cavity flow, are not perfectly coherent, as shown in Fig. 13.

In Fig. 24, the spatial variations in the amplitude of the fluctuations in  $u_2$  for the excitation frequency for the backstep flows with and without the artificial acoustic source of  $A/\rho_\infty=3.0\times 10^{-5}$  are compared with the corresponding variation for the cavity flow. It is clarified that the spatial variation in the region of  $0\leq x_1/2H\leq 0.3$  is approximately the same as that in the corresponding region for the cavity flow. Therefore, it is concluded that the acoustic feedback in the cavity flow is also reproduced in the backstep flow with the artificial acoustic source of  $A/\rho_\infty=3.0\times 10^{-5}$  in addition to the acoustic field, for which a detailed discussion is given in Sec. IV E 3.

### 3. Acoustic feedback

Figure 25 shows the variation in the PSD of  $u_{2c}$  and that of  $u_{2p}$  for the excitation frequency along  $x_2=0$  for the backstep flow with  $A/\rho_\infty=3.0\times 10^{-5}$ , where  $u_{2c}$  and  $u_{2p}$  represent the convective and propagative components of  $u_2$ , respectively,

$$u_2 = u_{2c} + u_{2p}. \quad (20)$$

The propagative component  $u_{2p}$  is assumed to be the same as particle velocity, which was calculated for the acoustic propagation around the backstep from the same artificial acoustic source without flow. The convective component  $u_{2c}$

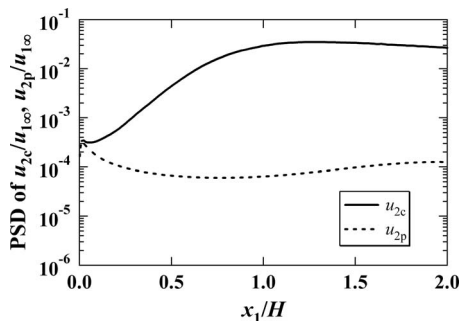


FIG. 25. Variations in PSD of convective component  $u_{2c}/u_{1\infty}$  and propagative component  $u_{2p}/u_{1\infty}$  of vertical velocity along  $x_2=0$  for backward-facing step flows with acoustic source.

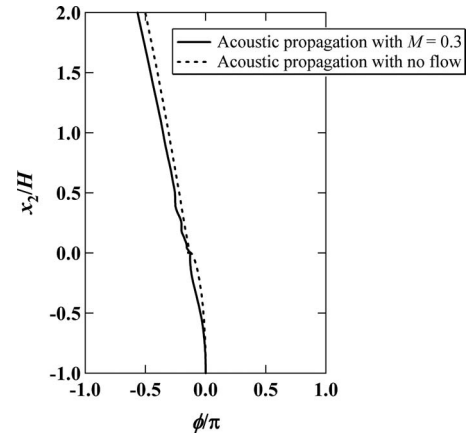


FIG. 26. Phase variations in pressure along  $x_1=0$  for backward-facing flows with artificial acoustic source for  $M=0.3$  and no flow.

is obtained by subtracting the propagative component from the computed velocity for the backstep flow of  $M=0.3$ . In Fig. 26, the spatial variation in the pressure phase on the vertical wall ( $x_1=0$ ) for this backstep flow is compared with that of the acoustic field around the backstep from the same acoustic source without flow. The acoustic field of the backstep flow with  $M=0.3$  is in good agreement with that without flow. This confirms that the effects of the mean flow on the acoustic propagation are negligibly small. Figure 25 shows that the propagative disturbances caused by the acoustic waves are negligibly small in comparison to the convective disturbances caused by the large-scale vortices in the region  $x_1/H>0.2$ .

Figure 27 shows the variations in the PSD of  $u_{2c}$  for the excitation frequency along  $x_2=0$  for backstep flows with and without an artificial acoustic source compared with that predicted by the LSA. For the backstep flow without an acoustic source,  $u_{2c}$  is equal to  $u_2$ . Only the curve predicted by the LSA for the backstep flow without an acoustic source is shown because the result of the LSA is virtually independent of the strength of the acoustic source. As shown in Fig. 27, the convective disturbances become more intense as the artificial sound becomes more intense. However, all the three amplification rates computed from the present LES data approximately agree with that predicted by the LSA in the region  $0.2\leq x_1/H<0.4$ . This means that the growth of the con-

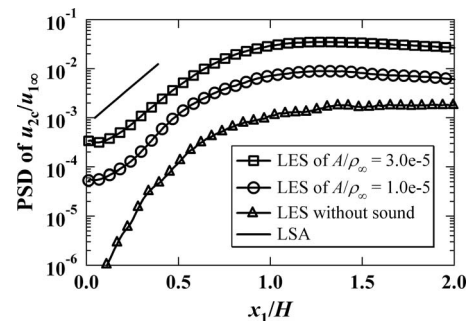


FIG. 27. Variations in PSD of convective component  $u_{2c}/u_{1\infty}$  of vertical velocity along  $x_2=0$  for backward-facing step flows with and without acoustic source.

vective disturbances is due to the KH instability and not affected by the acoustic waves. Meanwhile, the acoustic waves induce the initial convective disturbances as mentioned below. As already shown in Fig. 21, the acoustic waves are propagated around the upstream edge in the  $+x_2$  direction. As a result, the shear layer is moved up and down due to the particle velocity of the acoustic waves and the initial convective disturbances are generated in the shear layer. Therefore, the initial convective disturbances become more intense as the acoustic waves become more intense, as shown in Fig. 27.

Since the acoustic field and the acoustic feedback are reproduced in the backstep flow with the artificial acoustic source, the above discussion also holds for the acoustic feedback in the cavity flow. In the cavity, the initial convective disturbances are generated by the acoustic waves radiated due to the collision of the vortices on the downstream wall. These initial convective disturbances are coherent in the spanwise direction since the acoustic waves are coherent. These convective disturbances grow into the coherent large-scale vortices due to the KH instability independent of the acoustic waves and the fine-scale vortices, similar to those in a laminar cavity flow.<sup>9,10</sup>

## V. CONCLUSION

The fluid-acoustic interactions in a flow over a two-dimensional rectangular cavity were investigated by directly solving the compressible Navier–Stokes equations. The upstream boundary layer was turbulent. The depth-to-length ratio of the cavity was 0.5. Moreover, to clarify the acoustic feedback for the cavity flow in detail, the effects of artificial acoustic waves on the shear layer of a backstep flow with the same Mach number were also investigated.

Phase-averaged flow fields revealed the mechanism of the acoustic radiation in detail. Two-dimensional large-scale vortices composed of turbulent fine-scale vortices form in the shear layer that separates from the upstream edge of the cavity. When a large-scale vortex collides with the downstream wall, the low-pressure fluid in the vortex spreads along the downstream wall. As a result, a local downward velocity is induced by the local pressure gradient, and the upstream fluid expands. In this way, an expansion wave is radiated.

The large-scale vortices originate from the convective disturbances that are developed in the shear layer. The amplification rate of the convective disturbances agrees with that predicted by LSA. This means that the disturbances grow due to KH instability, similar to the growth of those in a laminar cavity flow. To clarify the mechanism for the generation of the initial convective disturbances, computations for backward-facing step flows with an artificial acoustic source were also performed. As the artificial acoustic waves became more intense, the initial convective disturbances in the shear layer became more intense while the amplification rate was not changed. This means that the initial convective disturbances in the shear layer are induced by the acoustic waves and developed into the large-scale vortices due to the KH instability independent of the acoustic waves and the

fine-scale vortices. This mechanism of the formation of the large-scale vortices also holds for the cavity flow.

The present study has provided much deeper understanding of the fluid-acoustic interactions in turbulent cavity flows, which should lead to improved design of various industrial products and the suppression of the effects of such interactions.

## ACKNOWLEDGMENTS

This research has been supported by a global COE program “Global Center of Excellence for Mechanical Systems Innovation” of the University of Tokyo and by a research program “Revolutionary Simulation Software” supported by the Ministry of Education, Culture, Sports, Science and Technology of Japan (MEXT).

- <sup>1</sup>K. Karamcheti, “Acoustic radiation from two-dimensional rectangular cut-outs in aerodynamic surfaces,” NACA Report No. TN 3487, 1955.
- <sup>2</sup>F. Mizushima, H. Takakura, T. Kurita, C. Kato, and A. Iida, “Experimental investigation of aerodynamic noise generated by a train-car gap,” *J. Fluid Sci. Technol.* **2**, 464 (2007).
- <sup>3</sup>P. Oshkai and T. Yan, “Experimental investigation of coaxial side branch resonators,” *J. Fluids Struct.* **24**, 589 (2008).
- <sup>4</sup>J. C. Bruggeman, A. Hirschberg, M. E. H. van Dongen, and A. P. J. Wijnands, “Self-sustained aeroacoustic pulsations in gas transport systems: Experimental study of the influence of closed side branches,” *J. Sound Vib.* **150**, 371 (1991).
- <sup>5</sup>J. E. Rossiter, “Wind-tunnel experiments on the flow over rectangular cavities at subsonic and transonic speeds,” Aeronautical Research Council Report No. 3438, 1964.
- <sup>6</sup>A. Powell, “On the edge tone,” *J. Acoust. Soc. Am.* **33**, 395 (1961).
- <sup>7</sup>L. F. East, “Aerodynamically induced resonance in rectangular cavities,” *J. Sound Vib.* **3**, 277 (1966).
- <sup>8</sup>D. Rockwell and E. Naudascher, “Review—self-sustaining oscillations of flow past cavities,” *ASME Trans. J. Fluids Eng.* **100**, 152 (1978).
- <sup>9</sup>C. Knisely and D. Rockwell, “Self-sustained low-frequency components in an impinging shear layer,” *J. Fluid Mech.* **116**, 157 (1982).
- <sup>10</sup>C. W. Rowley, T. Colonius, and A. J. Basu, “On self-sustained oscillations in two-dimensional compressible flow over rectangular cavities,” *J. Fluid Mech.* **455**, 315 (2002).
- <sup>11</sup>S. K. Lele, “Compact finite difference schemes with spectral-like resolution,” *J. Comput. Phys.* **103**, 16 (1992).
- <sup>12</sup>D. P. Rizzetta and M. R. Visbal, “Large-eddy simulation of supersonic cavity flow fields including flow control,” *AIAA J.* **41**, 1452 (2003).
- <sup>13</sup>C. Bogey and C. Bailly, “Large eddy simulations of round free jets using explicit filtering with/without dynamic Smagorinsky model,” *Int. J. Heat Fluid Flow* **27**, 603 (2006).
- <sup>14</sup>C. Bogey and C. Bailly, “Turbulence and energy budget in a self-preserving round jet: Direct evaluation using large eddy simulation,” *J. Fluid Mech.* **627**, 129 (2009).
- <sup>15</sup>K. Matsuura and C. Kato, “Large-eddy simulation of compressible transitional flows in a low-pressure turbine cascade,” *AIAA J.* **45**, 442 (2007).
- <sup>16</sup>D. V. Gaitonde and M. R. Visbal, “Padé-type higher-order boundary filters for the Navier–Stokes equations,” *AIAA J.* **38**, 2103 (2000).
- <sup>17</sup>K. W. Thompson, “Time dependent boundary conditions for hyperbolic systems,” *J. Comput. Phys.* **68**, 1 (1987).
- <sup>18</sup>T. J. Poinsot and S. K. Lele, “Boundary conditions for direct simulations of compressible viscous flows,” *J. Comput. Phys.* **101**, 104 (1992).
- <sup>19</sup>J. W. Kim and D. J. Lee, “Generalized characteristic boundary conditions for computational aeroacoustics,” *AIAA J.* **38**, 2040 (2000).
- <sup>20</sup>J. B. Freund, “Proposed inflow/outflow boundary condition for direct computation of aerodynamic sound,” *AIAA J.* **35**, 740 (1997).
- <sup>21</sup>J. Larsson, L. Davidson, M. Olsson, and L. Eriksson, “Aeroacoustic investigation of an open cavity at low Mach number,” *AIAA J.* **42**, 2462 (2004).
- <sup>22</sup>H. Yokoyama, Y. Tsukamoto, C. Kato, and A. Iida, “Self-sustained oscillations with acoustic feedback in flows over a backward-facing step with a small upstream step,” *Phys. Fluids* **19**, 106104 (2007).

- <sup>23</sup>J. O. Hinze, *Turbulence*, 2nd ed. (McGraw-Hill, New York, 1975), pp. 175–320.
- <sup>24</sup>J. Coupland, “Transition modeling for turbomachinery flows, T3 test cases,” ERCOFTAC Bulletin, No. 5, 1990.
- <sup>25</sup>S. K. Robinson, “Coherent motions in the turbulent boundary layer,” *Annu. Rev. Fluid Mech.* **23**, 601 (1991).
- <sup>26</sup>T. L. Jackson and C. E. Grosch, “Inviscid spatial stability of a compressible mixing layer,” *J. Fluid Mech.* **208**, 609 (1989).
- <sup>27</sup>M. Zhuang, T. Kubota, and P. E. Dimotakis, “Instability of inviscid, compressible free shear layers,” *AIAA J.* **28**, 1728 (1990).
- <sup>28</sup>C. K. W. Tam and J. C. Hardin, Second Computational Aeroacoustics (CAA) Workshop on Benchmark problems, NASA, CP 3352 (1997).